Geo-Mar Lett (2011) 31:123–140
DOI 10.1007/s00367-010-0220-0

ORIGINAL

Near-surface electromagnetic, rock magnetic, and geochemical fingerprinting of submarine freshwater seepage at Eckernförde Bay (SW Baltic Sea)

Hendrik Müller · Tilo von Dobeneck · Wiebke Nehmiz · Kay Hamer

Received: 2 February 2010 / Accepted: 2 September 2010 / Published online: 5 October 2010

Abstract Submarine groundwater discharge in coastal settings can massively modify the hydraulic and geochemical conditions of the seafloor. Resulting local anomalies in the morphology and physical properties of surface sediments are usually explored with seismo-acoustic imaging techniques. Controlled source electromagnetic imaging offers an innovative dual approach to seep characterization by its ability to detect pore-water electrical conductivity, hence salinity, as well as sediment magnetic susceptibility, hence preservation or diagenetic alteration of iron oxides. The newly developed electromagnetic (EM) profiler *Neridis II* successfully realized this concept for a first time with a high-resolution survey of freshwater seeps in Eckernförde Bay (SW Baltic Sea). We demonstrate that EM profiling, complemented and validated by acoustic as well as sample-based rock magnetic and geochemical methods, can create a crisp and revealing fingerprint image of freshwater seepage and related reductive alteration of near-surface sediments. Our findings imply that (1) freshwater penetrates the pore space of Holocene mud sediments by both diffuse and focused advection, (2) pockmarks are marked by focused freshwater seepage, underlying sand highs, reduced mud thickness, higher porosity, fining of grain size, and anoxic conditions, (3) depletion of Fe oxides, especially magnetite, is more pervasive within pockmarks due to higher concentrations of organic and sulfidic reaction partners, and (4) freshwater advection reduces sediment magnetic susceptibility by a combination of pore-water injection (dilution) and magnetite reduction (depletion). The conductivity vs. susceptibility biplot resolves subtle lateral litho- and hydrofacies variations.

H. Müller (✉) · T. von Dobeneck · K. Hamer
MARUM—Center for Marine Environmental Sciences and
Faculty of Geosciences, University of Bremen,
Klagenfurter Strasse,
28359 Bremen, Germany
e-mail: hendrik.mueller@uni-bremen.de

W. Nehmiz
FIELAX Gesellschaft für wissenschaftliche
Datenverarbeitung mbH,
27568 Bremerhaven, Germany

Introduction

Freshwater seepage from terrestrial aquifers contributes significantly to the mass exchange of coastal seas. Inlets with minor river input such as Eckernförde Bay (northern Germany, SW Baltic Sea) can receive 40% or more of their freshwater influx from submarine groundwater discharge (Moore 1996; Schlüter et al. 2004). Besides water balance and chemistry, sedimentary redox states and element cycles are strongly influenced by freshwater advection or chemical reactions coupled to seawater recirculation through a coastal aquifer system (Burnett et al. 2001).

Onshore, aerogeophysical methods, especially helicopter-based electromagnetic (EM) surveying, are comprehensively used to map aquifer structures, to delineate soil and groundwater salinization, saltwater intrusion into coastal aquifers, and the geology of coastal areas (e.g., Siemon 2006; Steuer et al. 2007). However, offshore mapping of the spatial patterns of submarine freshwater expulsion is mainly the domain of acoustic methods. Focused fluid flow through the seabed produces characteristic geomorphologic expressions such as pockmarks, distorted stratification, impedance contrasts, and backscatter effects (Jensen et al. 2002; Hovland 2003). Ground-truthing is typically performed with schlieren optics (Karpen et al. 2004), benthic habitat mapping, in-situ seepage meters, and pore-water

sampling and analysis (Burnett et al. 2006). These techniques are restricted to sites with favorable geological and hydrological conditions.

Hoefel and Evans (2001) demonstrated that EM induction methods are also suitable for imaging sub-seafloor freshwater seeps and aquifers, due to their much lower salinity and electrical conductivity σ. The complex response of a sedimentary half-space to an EM field is composed of an out-of-phase (or quadrature) signal representing electrical pore-water conductivity σ, and an in-phase signal driven by the magnetic permeability μ (or magnetic susceptibility κ with $\kappa=\mu-1$) of the sedimentary matrix. At very low operating frequencies f (~25–100 Hz), the contribution of conductivity to this in-phase signal can be neglected (Farquharson et al. 2003; Won and Huang 2004). Controlled source electromagnetic (CSEM) sounding allows separation of magnetic and electrical signal components from the low- and high-frequency parts of a single multi-frequency EM measurement at high sensitivity.

In rocks and sediments, the magnetic susceptibility κ depends primarily on their content of strongly (ferri-) magnetic oxidic and sulfidic iron mineral phases such as (titano-)magnetite ($Fe_{3-x}Ti_xO_4$) and greigite (Fe_3S_4; Thompson et al. 1980; Verosub and Roberts 1995). Such magnetic minerals are unique in that they can be detected using rapid rock magnetic bulk sediment analyses with paleomagnetic laboratory equipment, as well as by various magnetic remote detection methods used in geophysical ore exploration.

The magnetic petrology of marine deposits is indicative of sediment provenance, grain size, and redox state, and often mirrors climatic, hydrodynamic and/or anthropogenic influences (Zhang et al. 2001; Tribovillard et al. 2002; Emiroglu et al. 2004; Funk et al. 2004; Rey et al. 2005; Ellwood et al. 2006). Depletion of redox-sensitive iron oxides under reducing, especially sulfidic conditions is a widely observed early diagenetic phenomenon. Ti-poor magnetite and, at slower pace, hematite (Fe_2O_3) dissolve under suboxic and anaerobic conditions, in particular under sulfidic conditions (Dillon and Bleil 2006) to reprecipitate either as weakly paramagnetic (FeS, FeS_2) or as strongly ferrimagnetic (Fe_3S_4, Fe_9S_{11}) iron sulfides (Rowan and Roberts 2006; Fu et al. 2008). Magnetic enhancement and depletion by remineralization has therefore been identified as a tracer of hydrothermal venting (Tivey and Johnson 2002) and methane accumulation in sediments (Housen and Musgrave 1996; Novosel et al. 2005; Larrasoaña et al. 2007). However, little is known about magnetic mineral alterations and related susceptibility changes caused by submarine groundwater discharge, and their potential detectability by geophysical methods.

Conventional laboratory alternating field susceptometers do not operate properly in a highly conductive seawater environment (Benech and Marmet 1999; Müller 2010). Passive marine Overhauser or cesium magnetometers require relatively sharp lateral magnetization contrasts, and cannot resolve the subtle magnetic anomalies of hydrogeologically altered Holocene subsurface sediments from the more prominent background signals created by heterogeneous deeper glacial strata or the crystalline basement (Gay 2004). To overcome these technical problems, a new bottom-towed marine profiler Neridis II (NERItic DIScoverer) carrying a commercial multi-frequency EM sensor was developed in cooperation between the MARUM Center for Marine Environmental Sciences at the University of Bremen, Germany and the Marine and Environmental Geology Group (MARGO) at the University of Vigo, Spain (Rey et al. 2008; Müller 2010). Sizes, arrangement, and operation frequencies of the EM sensor coils were optimized for synchronous magnetic susceptibility and electrical conductivity measurements of the near-surface sediment (90% signal from 0-50 cm sub-bottom depth). The system reaches sub-meter lateral resolution at sampling rates of 25 samples per second and tow speeds of 3–4 knots in both shallow- (5–50 m) and deepwater (50–500 m) operations.

This Eckernförde Bay case study has been conducted in a previously well-studied cold seep area with numerous characteristic pockmark structures. Beside high-resolution EM profiling and sampling, detailed rock magnetic and geochemical analyses of near-surface sediments were performed to validate the seafloor measurements, to expand them by analytical geochemical and rock magnetic parameters, and to clarify relevant geological signal formation processes. Specifically, this study aims to (1) investigate the impact of focused and diffuse submarine groundwater seepage on the porosity, pore-water conductivity, and magnetic mineralogy of marine surface sediments, (2) document how electrical conductivity and magnetic susceptibility data can be combined to distinguish and characterize hydraulic and diagenetic regimes, (3) test the performance of the novel EM profiler in a logistically simple, but geologically complex near-shore setting, and (4) demonstrate the potential of combining high-resolution EM mapping with environmental magnetic and geochemical laboratory analytics.

Study area

Eckernförde Bay is a 16-km-long and 2–6 km wide funnel-shaped inlet of glacial origin situated on the east coast of Schleswig-Holstein (northern Germany) in the southwestern Baltic Sea (Fig. 1). Medium to fine sands predominate on the slopes above the wave base at 22 m water depth, while the center of the 26–28 m deep bay is covered by

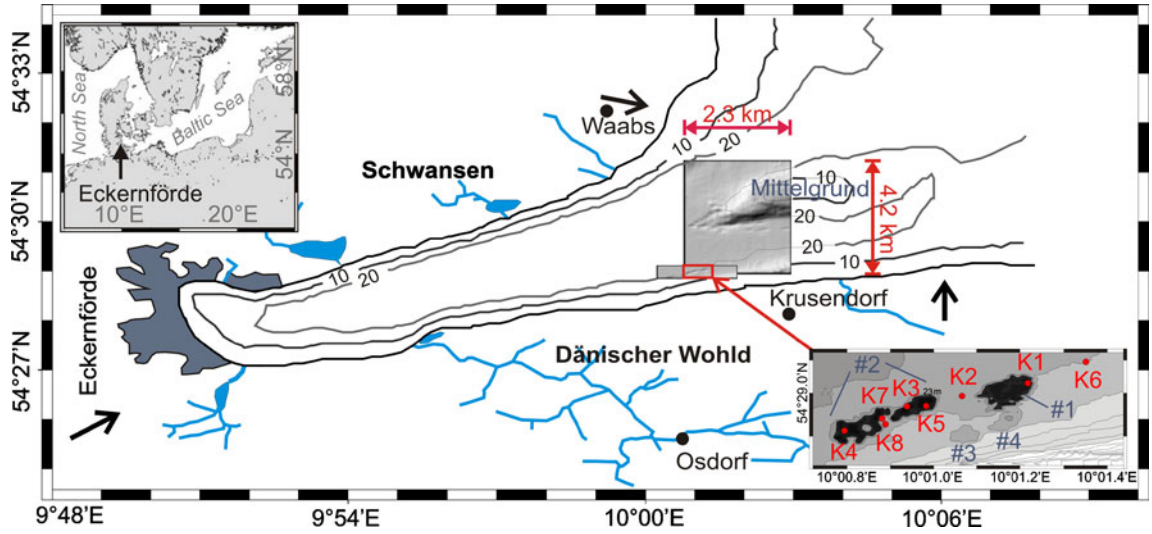

Fig. 1 Map of Eckernförde Bay with 10- and 20-m isobaths, and more detailed bathymetries of the 'Mittelgrund' and southern bay slope freshwater seepage area (shaded relief maps). Freshwater feeders (*blue lines*) and groundwater flow directions (*black arrows*) are extracted from Marczinek and Piotrowski (2002). The close-up on the lower right-hand side depicts the locations of cores K1–K8, and of pockmark #1 near core K1 and pockmark #2 near cores K3–K5, K7, K8. Two smaller and shallower depressions #3 and #4 are located south of core K2 and pockmark #1

mud with a median grain size of 15–20 μm and low hydraulic permeabilities of 10^{-13} to 10^{-15} m^2 (Schlüter et al. 2004). High sedimentation rates of 1.4 mm/year and loads of 4–5 dry wt% total organic carbon (TOC) lead to the development of anoxic conditions within the uppermost few centimeters of the sediments, and of extensive zones of sulfate reduction and methanogenesis in the Holocene mud layer (Whiticar 2002). Several pockmark depressions of 1–2 m depths with lateral extents of 50–300 m have been identified on the southern bay slope and the 'Mittelgrund', an elongated moraine sill in the center of the bay (Jensen et al. 2002). Sediments within the pockmark structures have low pore-water chloride concentrations and gently undulating sediment–water interfaces (Schlüter et al. 2004). Vertical pore-water salinity gradients show non-steady-state characteristics that indicate episodic freshwater seepage (Whiticar 2002).

The hydrogeological setting is characterized by two connected aquifers that are confined in a Miocene lignite sand and a Pleistocene glacio-fluviatile sand horizon embedded between till complexes; the hydrostatic head is 1–2 m above sea level (Marczinek and Piotrowski 2002). Heavy rainfalls as well as strong westerly offshore winds can trigger episodic groundwater outflow by overbalancing the hydraulic state of the aquifers (tides are negligible in the Baltic Sea). The interplay of fluid seepage and bottom currents is considered responsible for the formation and preservation of pockmarks (Whiticar and Werner 1981; Harrington 1985; Schlüter et al. 2004). Due to long flow paths from its southern sources, the groundwater arrives in a highly reduced chemical state (Marczinek and Piotrowski 2002). The intermixing of the groundwater and the brackish seawater of the SW Baltic Sea (mean chloride concentration of 12‰, up to 14‰; Whiticar 2002) is expected to occur close to the sediment–water interface. Deep-towed CTD profiling in a previous study (Schlüter et al. 2004), however, could not find freshwater plumes in the water column.

Materials and methods

Three dedicated sampling and survey campaigns with RB *Polarfuchs* (IFM-GEOMAR, Kiel) were performed in the summers of 2006 and 2008. A first survey in May 2006 focused on the hydroacoustic and magnetic mapping of two known pockmark areas (Jensen et al. 2002) along the Mittelgrund (50-m-spaced N–S profiles, and 250-m-spaced E–W tie-lines within a 4.2×2.3 km area) and the southern bay slope (25-m-spaced E–W profile lines, and 125-m-spaced N–S tie-lines covering an area of 1.2×0.4 km). Sediment samples were taken in the southern working area during a second campaign in August 2006 (Nehmiz 2007). EM and hydrographic surveys with the new bottom-towed profiler Neridis II were performed over 3 days in July 2008. Two overlapping grids in a 1.4×0.5 km area comprised 25 E–W profiles of 20-m line spacing, and four unequally spaced N–S tie-lines, all surveyed at typical tow speeds of 2–3.5 knots.

Hydroacoustic and magnetic surveys

Hydroacoustic and marine magnetic surveys were performed in the same area to establish a high-resolution

bathymetry of the Holocene mud drape and underlying glacial substratum. A 10-kHz SyQuest StrataBox™ acoustic sub-bottom profiler was towed in a non-magnetic rubber dinghy with DGPS positioning at a distance of 100–120 m behind RB *Polarfuchs*. A GEM systems GSM-19 marine Overhauser magnetometer was alternatively (1) mounted in the dinghy, (2) towed at ca. 4 m above the seafloor, or (3) bottom-towed on a nonmagnetic sled. In modes (2) and (3), the magnetometer and dinghy had identically adjusted laybacks that permitted determination of the position and depth of the magnetometer from the DGPS and echosounder on the boat.

Seafloor and sub-bottom reflector depths were selected from the sub-bottom profiler sections and gridded with a Geosoft Oasis Montaj 7.1 Minimum Curvature algorithm. Magnetic data were corrected for diurnal drift with a shore-based Proton magnetometer station, resampled at 1-m spacing, bandpass filtered in the periodicity range of 30–4,000 m, leveled, and inverted to apparent subsurface magnetizations using the method of Hussenoeder et al. (1995).

Electromagnetic and hydrographic surveys

The application of CSEM in shallow marine studies is relatively new and has so far been restricted to the detection of metallic objects such as unknown ordnance by Won and Huang (2004). We used their GEM-3 broadband, frequency domain electromagnetic induction sensor (Won et al. 1997; distributed by Aeroquest Sensortech Ltd., formerly Geophex) in a submarine modification where the concentric and coplanar transmitter coil (Ø 96 cm), bucking coil (Ø 53 cm), and receiver coil (Ø 30 cm) were wound into an oil-filled PVC casing (Müller 2010). The bucking coil compensates the direct signal of the transmitter coil at the position of the receiver coil in order to exclusively record the weak secondary EM fields of the currents induced to the conductive seawater and seafloor surroundings (quadrature signal), and the induced magnetizations of magnetic subsurface minerals and objects (in-phase signal).

The GEM-3 sensor was mounted into the custom-built nonmagnetic and non-conductive Neridis II fiberglass sled (Fig. 2). Positioned at a distance of 20 cm above the seafloor, the sensitivity of the sensor decays exponentially with sub-bottom depth, such that 90% of the signal integrates over the uppermost 50 cm of sediment. The sled was further equipped with two CTDs, an internal Seabird SBE 16 and external Sea&Sun CTD 48 positioned 0.75 m above ground, an electronic compass, roll and pitch motion sensors, an embedded PC, and lead-battery power supply. Real-time data transmission to the tow boat was realized by DSL network telemetry via the armored coaxial tow cable. The position of the sled was determined with an estimated

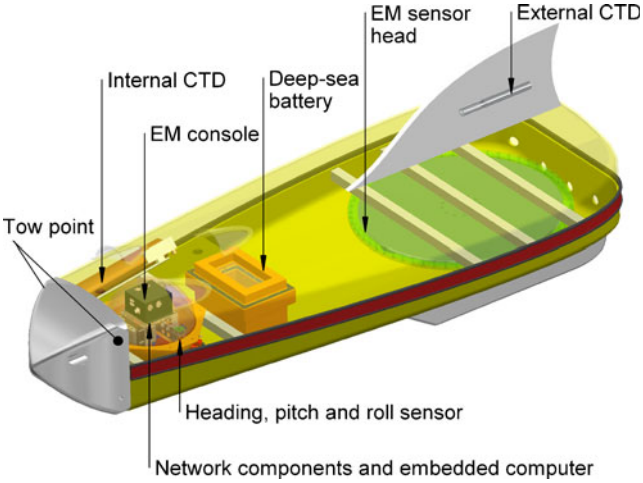

Fig. 2 Setup of the EM profiler Neridis II (NERitic DIScoverer). The 3.6-m-long, 1.2-m-wide, and 0.6-m-high sled (fin: 1.0 m high) consists of two symmetrical fiberglass shells (the upper shell is drawn transparent), a concrete nose, concrete vats with PVC runners, and a PVC fin. The concentric coplanar EM coils are located in a solid disc (*green*) toward the tail end, and a spherical glass pressure housing, internal CTD, and 24V DC battery near the nose; seawater flushes through vents in the nose and tail

precision of ~5 m from the tow boat's DGPS position, the horizontal layback, and the compass course of the sled. The applied lag distance was verified from reverse control profiles. The multi-frequency transmitter waveform was created by superimposing frequencies of 75, 175, 525, 1,025 and 4,775 Hz with a pulse-width modulation technique (Won et al. 1997), and amplified to a peak transmitter moment of 61 Am^2. EM data were gathered at 25-Hz sampling rate and low-pass filtered at 5 Hz to reduce intrinsic noise. Towed at speeds of 2–3.5 knots, the system achieves an effective lateral resolution of ca. 20–35 cm. EM sensor drift was corrected by interpolating between water-column background measurements taken after every second profile.

The electrical conductivity and magnetic susceptibility of the subsurface sediments were calculated with a half-

Fig. 3 **a**–**f** Acoustic, hydrographic, and electromagnetic maps of the ▶ southern bay slope survey area (data gridded with a minimum curvature algorithm, and shown with linear color scales shaded from the NE and overlain by bathymetric contour lines of 0.5-m spacing; *white line* section of Fig. 4). **a** Bathymetry (CTD pressure data) and EM profile lines (*blue*); **b** bottom-water electrical conductivity measured using the profiler's external CTD; **c** mud layer thickness and **d** sand reflector depth, both determined from 10-kHz sub-bottom profiles; **e** apparent electrical conductivity and **f** apparent magnetic susceptibility, calculated from the 4.8-kHz quadrature and 75-Hz in-phase EM signals, respectively. **g**, **h** Deep-towed passive Overhauser magnetometry and surface sample maps of the survey area. **g** Magnetization of the subsurface related to a virtual layer of 10-m thickness; **h** magnetic susceptibility of 146 surface grab samples (*yellow crosses*). *Orange circles* 17 sample locations for detailed rock magnetic and geochemical investigations, *black dots* gravity core locations K1 to K8 (note that K6 is located NE of K1, outside the map area)

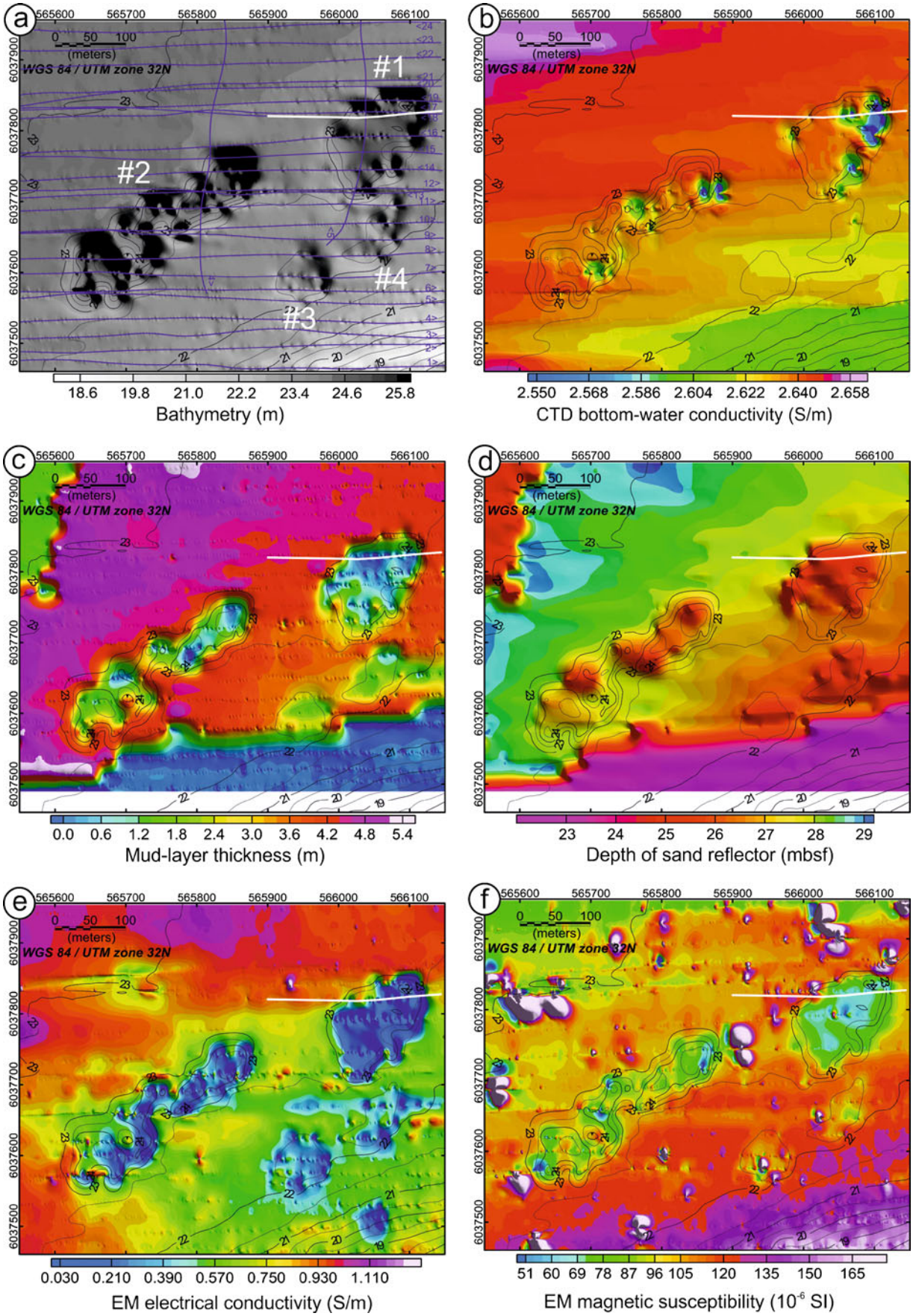
a
b
c
d
e
f
565600 565700 565800 565900 566000 566100
6037900 6037800 6037700 6037600 6037500
0 50 100
(meters)
WGS 84 / UTM zone 32N
#1
#2
#3
#4
18.6 19.8 21.0 22.2 23.4 24.6 25.8
Bathymetry (m)
2.550 2.568 2.586 2.604 2.622 2.640 2.658
CTD bottom-water conductivity (S/m)
0.0 0.6 1.2 1.8 2.4 3.0 3.6 4.2 4.8 5.4
Mud-layer thickness (m)
23 24 25 26 27 28 29
Depth of sand reflector (mbsf)
0.030 0.210 0.390 0.570 0.750 0.930 1.110
EM electrical conductivity (S/m)
51 60 69 78 87 96 105 120 135 150 165
EM magnetic susceptibility (10-6 SI)

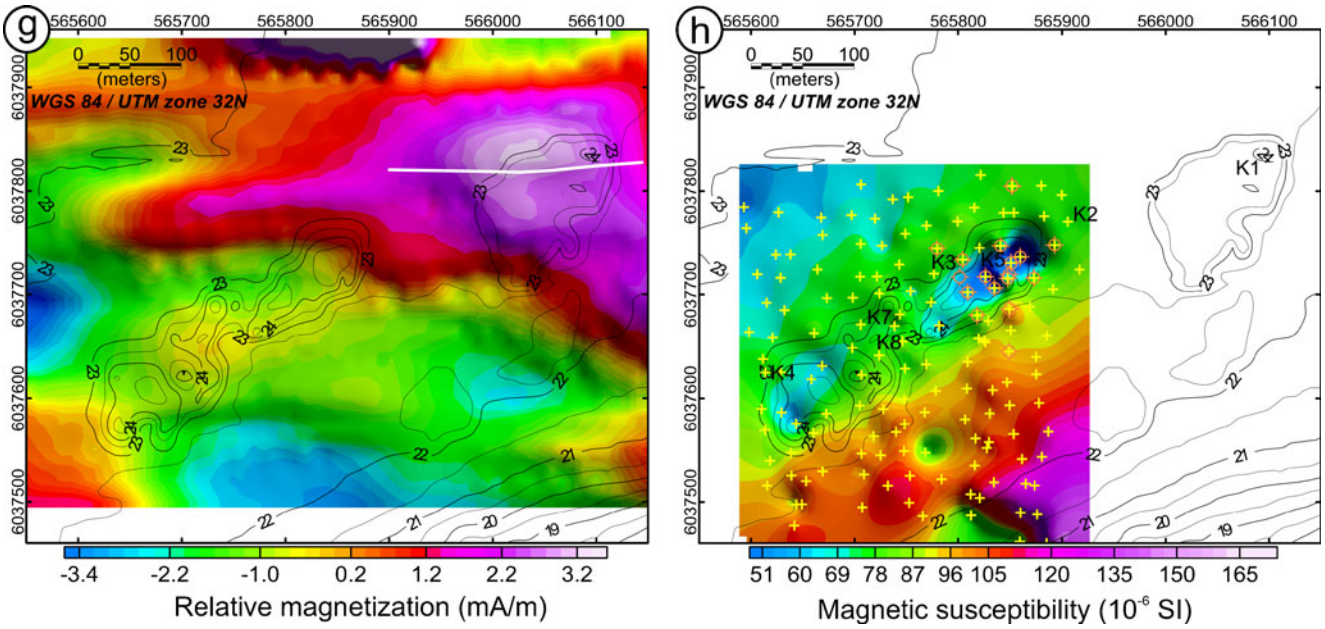

Fig. 3 (continued)

space inversion algorithm (Müller 2010) based on seawater conductivity data of the internal CTD. Conductivity was determined from the 4,775-Hz quadrature component of the secondary EM field, and susceptibility from the 75-Hz in-phase component. The subsurface conductivity signal was used to subtract its (minor) contribution to the in-phase signal. The 4-Hz conductivity, temperature, and pressure data from the external CTD were used to calculate bottom-water salinity and to establish a cm-resolution along-track bathymetry.

Sediment sampling

Eight gravity cores (K1–K8) of 30 to 60 cm lengths were taken with a Rumohr gravity corer along a transect across pockmarks #1 and #2 in the southern study area (Figs. 1 and 3h). The cores were cold-stored (4°C), and within 24 h sub-sampled at 2-cm intervals into 6.2-cm^3 plastic cubes for laboratory rock magnetic investigation. The remainder of the sediment was prepared for element and organic carbon analysis. Pore water from the bottom of each core was extracted with rhizone samplers (Seeberg-Elverfeldt et al. 2005) for laboratory salinity determination with a sensION 5 conductivity meter calibrated to NaCl standards.

In addition, 146 samples of at least 500 cm^3 were collected from the uppermost 5–6 cm of the seabed with a 25×25 cm Van Veen grab sampler on a 25-m mesh grid covering an area of 270×270 m around pockmark #2 (Fig. 3h). These were filled into 500-cm^3 plastic bottles for bulk magnetic susceptibility measurements using a Bartington Instruments MS2C loop sensor, which was calibrated for the specific bottle size with a MnCl standard. A subset of 15 surface samples covering the NE part of pockmark #2 and its surroundings were homogenized by stirring, and sampled for rock magnetic and geochemical analyses in the same way as the core samples.

Rock magnetic analyses

Bulk rock magnetic measurements were applied to all gravity cores at 2-cm intervals and to the surface samples. Low-field magnetic susceptibility (κ) was measured with a Bartington Instruments MS2D susceptibility meter. An anhysteretic remanent magnetization (ARM) was imparted in a 100-mT AF field and 40-μT DC biasing field, and was subsequently AF demagnetized in 11 steps to determine its median destructive field (MDF). The ARM was measured in a 2G Enterprises 755R DC SQUID pass-through cryogenic magnetometer, and is used as an indicator of the concentration of sub-micron magnetite (King et al. 1982; Thompson and Oldfield 1986; Oldfield and Yu 1994). An isothermal remanent magnetization (IRM) was imparted and measured at five incremental steps up to a 700-mT peak field with a pulse magnetizer and the 2G Enterprises 755R magnetometer. The IRM at this maximum field was considered to be the saturation IRM (SIRM), and was used with the 300-mT IRM to calculate the 'hard' IRM (HIRM) that represents the content of high-coercivity minerals such as hematite and goethite (King and Channell 1991; Bloemendal et al. 1992; Maher and Thompson 1999). The ARM/SIRM ratio quantifies the relative concentration of the clay-size single domain (SD) fraction, and is widely used for magnetic granulometry (Evans and Heller 2003). The SIRM/κ ratio is also used in magnetic granulometry, but focuses more on grain-size variations of the silt-size multi-domain (MD) fraction. The $S_{0.3T}$ ratio given by the equation

$S_{0.3T}$=$IRM_{0.3T}$/SIRM measures variations in the relative content of high- and low-coercivity minerals in a range from 0 to 1 (King and Channell 1991; Maher and Thompson 1999). Magnetic hysteresis and backfield measurements up to a 300-mT peak field were performed with a Princeton Measurements Corporation M2900 alternating gradient magnetometer to determine the saturation magnetization M_s, remanent saturation magnetization M_{rs}, coercive force B_c and coercivity of remanence B_{cr}, all of which specify characteristics of ferrimagnetic mineral components.

Low-temperature diagnostics of magnetic mineralogy and domain state (e.g., Dunlop and Özdemir 1997; Housen and Moskowitz 2006) including (1) zero field cooling (ZFC) from 300 to 5 K prior to applying a 7-T field and warming back to 300 K, (2) field cooling (FC) from 300 to 5 K in a 7-T field and warming back to 300 K, (3) zero field cycling of a 7-T room temperature (RT-)SIRM from 300 to 5 K and back to 300 K, and (4) hysteresis measurements up to a 7-T peak field at 5 and 300 K were performed on a superconducting Quantum Design XL7 magnetic properties measurement system (MPMS).

Geochemical analyses

Elemental analyses were performed on freeze-dried and finely ground ~3 g samples using a SPECTRO XEPOS energy dispersive polarization X-ray fluorescence analyzer (EDP-XRF) calibrated to an alluvial mud standard that is representative of the sampling area. Total organic carbon (TOC) was quantified on 600 mg sub-samples that were treated twice with 12.5% HCl, using a LECO CS-200 carbon/sulfur analyzer. TOC values are reported in terms of dry wt% of bulk sediments.

Results

Acoustic, hydrographic, and electromagnetic profiling

The survey area in the 18–25 m water depth range encloses the transition from the muddy central basin to the gently inclined (ca. 2°) and more sandy southern slope of outer Eckernförde Bay (Fig. 3a). The depicted 600×500 m bathymetric section contains four discrete, morphologically distinct pockmarks #1 to #4. Pockmark #1 in the NE has the structure of a roundish trough, a size of 160×95 m, and a maximum depth of 2 m below the surrounding seafloor. Pockmark #2 in the SW is elongated in the ENE–WSW direction, and has a size of 340×100 m and a maximum relative depth of 1.5 m. Two smaller and shallower (0.7 m) depressions #3 and #4 are located south of pockmark #1 at the foot of the slope (rise). To give a better idea of the structural details, an expanded W–E section of pockmark #1 is shown in Fig. 4a.

Bottom-water conductivities given by the external CTD of the EM profiler (Fig. 3b) vary by 2% between 2.61 and 2.66 S/m, and systematically increase with water depth. Several localized highly negative conductivity anomalies of peak values up to 250 mS/m were observed especially in the eastern parts of pockmarks #1 and #2 (Figs. 3b, 4b), indicating freshwater admixture by active groundwater seepage. The preferred orientation of the low-conductivity anomalies at the eastern margins of the pockmarks may result either from a groundwater flow from the SE or else from a western bottom current.

A high-amplitude acoustic sub-bottom reflector marks the boundary of the Holocene mud drape (Fig. 3c) and glacial sand (Fig. 3d). The reflector depth could be well determined from the 10-kHz sub-bottom profiles except for the NW corner of the survey area, where acoustic turbidity by free gas limits sound penetration to 2–3 m below seafloor (mbsf). The thickness of the Holocene drape averages 3–4 m, and reaches a maximum of 5 m in the NW of the survey area (Fig. 3c). Inside the pockmarks, the mud layer is considerably thinner (0.3–1.5 m as verified by gravity coring) and undulates slightly, while the underlying sand formation bulges up to 3 m above its surrounding level (Figs. 3d, 4c). The lateral extent of this ‘sand high’ in pockmark #1 follows largely the shape of the depression except for the southern end of the structure. In contrast, sand highs of pockmark #2 are not as coherent and seem to form a chain of separate subunits, which may correspond to adjacent seeps. As the bulging of the sand reflector is always over-compensated by the thinning of the mud layer, the resulting seafloor relief remains negative.

The EM-based electrical conductivity of the seafloor (Figs. 3e, 4d) is principally controlled by pore-water salinity and temperature, as well as by (grain size-related) sediment porosity. The background value increases by 30% from 0.8 to 1.1 S/m within the investigated depth range, which indicates a fining of the sediment matrix with distance from shore. Inside the pockmarks, subsurface conductivity values decrease to less than 0.4 S/m (Fig. 3e). The resistive anomalies of pockmarks #1 and #2 strictly follow their morphologies, while the signatures of the smaller pockmarks #3 and #4 seem more diffuse. A fifth conductivity minimum of confined shape is situated on the sandy lower slope in the SE corner of the survey area. The absence of a pockmark depression related to this potential seep site could result from the local absence of a mud cover. The expanded W–E section (Fig. 4d) illustrates the local character of the subsurface conductivity minima, and points to the existence of separate groundwater vents at typical lateral distances of ~10–15 m. The slightly negative value of the easternmost conductivity peak is a processing artifact resulting from the very heterogeneous seawater half-space.

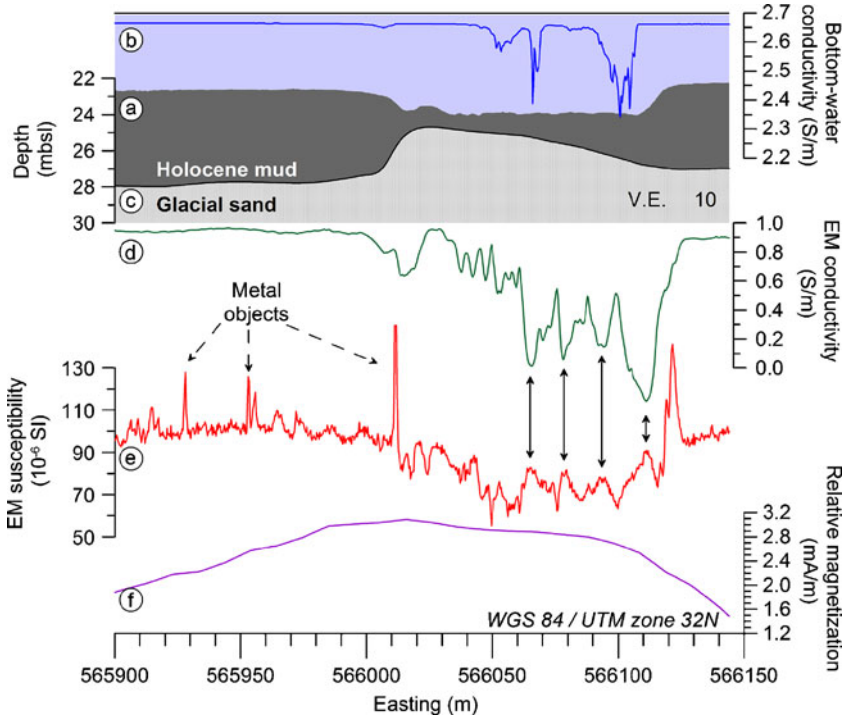

Fig. 4 E–W profile across pockmark #1 (see Fig. 3a–g). **a** Bathymetry and **b** bottom-water conductivity are given by the external CTD's pressure and conductivity sensors; **c** the depth of the glacial sand reflector was extracted from Fig. 3d. **d** Apparent electrical conductivity and **e** apparent magnetic susceptibility were calculated from EM signals; counter-phase conductivity minima and susceptibility maxima are marked by *black arrows*. Ferromagnetic objects are associated with distinct peaks in magnetic susceptibility. **f** The relative subsurface magnetization deduced by numerical inversion from Overhauser magnetometry has a positive anomaly below pockmark #1, and is therefore inverse to the subsurface susceptibility signal

The EM-based magnetic susceptibility map (Fig. 3f) outlines the above-described structures surprisingly well by virtue of contrasting magnetic iron mineral contents and excellent sensitivity of the EM sensor. As a general trend, susceptibility decreases from 160 to 70×10^{-6} SI with distance from shore. Numerous small positive point anomalies (spikes) probably reflect metallic subsurface contaminants. Sediments inside the pockmarks have up to 50% lower susceptibilities than the surrounding basin (Fig. 3d). The susceptibility minimum of pockmark #1 is uniform and conforms well to the shape of the bathymetric low, while the anomaly of pockmark #2 is composed of several smaller and less pronounced minima. The expanded W–E section (Fig. 4e) indicates generally lower susceptibilities in and around the pockmarks, while internal signal undulations are counter-phased with conductivity, which suggests iron precipitation at the vent sites.

The filtered anomaly pattern detected by deep-towed passive magnetometry (Figs. 3g, 4f) has smoother and essentially inverted anomaly features. The broad and positive anomalies over the pockmarks should therefore correspond to deeper, more strongly magnetic bodies, which seem to coincide with the observed glacial sand highs, but also with deeper structures.

The magnetic susceptibility map determined from surface sample measurements (Fig. 3h) is strikingly consistent with the EM image (Fig. 3f), in terms of both relative and absolute values. This finding is not self-evident, because of the different sediment depths (0–5 vs. 0–50 cm) represented by the two methods. The main difference between the sample-based and EM-based maps is the total lack of positive spikes (to be explained by the small chance of recovering small metallic objects by grab sampling) and the lower spatial resolution (due to the wider sampling grid). Again, susceptibility values within pockmark #2 are 35–50% lower than for adjacent areas, which indicates localized magnetic depletion of the Holocene mud under the influence of anoxic groundwater seepage.

Rock magnetic and geochemical analyses

Three hypothetic factors controlling EM signal formation (cf. above) were investigated by examining (1) reductive depletion of magnetite in and around pockmarks, (2) iron and magnetic mineral precipitation near groundwater seeps, and (3) high susceptibility contrasts between detrital magnetic minerals in Holocene muds and glacial sands. We present surface samples from a heterogeneous section of the NE part of pockmark #2 (Fig. 3h) where three pronounced low-conductivity spots coincide with susceptibility minima with remarkably different amplitudes, suggesting an interplay of the above mechanisms.

Down-core plots (Fig. 5c–j) and surface maps (Fig. 6a–c, f–i) are derived from selected diagnostic rock magnetic parameters and element contents of the 15 surface samples (0–5 cm), and three cores with distal (K2), proximal (K3), and central (K5) positions with respect to pockmark #2.

The stratigraphic perspective is more insightful in terms of signal formation processes, while the map-view depiction clarifies spatial and structural aspects. Down-core changes of susceptibility and conductivity are also crucial for the volume- and hence depth-integrating EM signal. In mathematical terms, the conductivity and susceptibility values derived by EM profiling correspond to a convolution of the applicable depth characteristic of the sensor and the true vertical distribution of these physical sediment properties.

The design and geometry of the sensor coils entail distinct depth characteristics for quadrature and in-phase signal components (Fig. 5a, b). Assuming a 100% response at the sediment–water interface, the sensitivity for conductivity (or susceptibility, respectively) reduces to 50% at a depth of 16 cm (17 cm) and to 10% at a depth of 71 cm (48 cm). In cumulative terms, the weight-averaged properties of the upper 0–21 cm (0–13 cm) correspond to 50%, and the upper 0–92 cm (0–48 cm) to 90% of the signal. No significant attenuation or reflection of the EM signal occurs in the relevant depth windows, because of sufficiently low sediment electrical conductivities and operating frequencies ('quasi-static approximation'). As the quadrature characteristic sensitivity changes marginally with frequency at the given sensing geometry, frequency domain depth inversion of the subsurface conductivity is excluded.

Sediment conductivity σ_{sed}, as described by Archie's Law (Archie 1942) $\sigma_{sed}=a\sigma_{water}\phi^{m}$ (with material constants a, m), is a physical expression of water-saturated sediment porosity ϕ and pore-water conductivity σ_{water}, itself controlled by salinity and temperature. Salinity and chloride content of pore water are nearly proportional. Dry bulk Cl^{-} content hence combines vertical porosity and salinity changes (Figs. 5c, 6a). While the gentle decline of Cl^{-} in the distal core K2 can possibly result from compaction alone, the strong curvature of the proximal and central profiles is typical of an interplay of episodic upward freshwater advection versus steady downward seawater diffusion (Whiticar 2002; Schlüter et al. 2004). Low chloride contents near the sediment surface indicate strong and/or recent freshwater seepage. From comparison of the quadrature sensitivity and Cl^{-} content curves, we estimate that the EM conductivity signal within the pockmarks integrates over 20–30% seawater and 70–80%

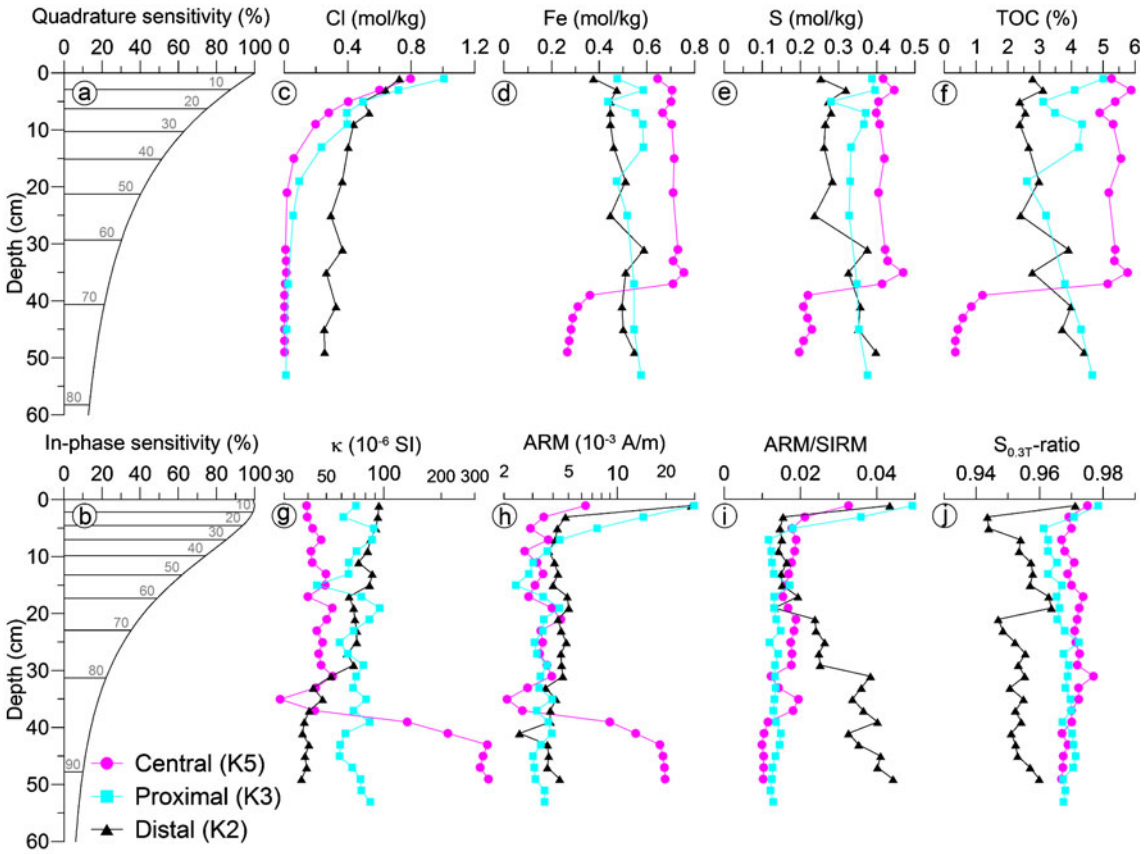

Fig. 5 EM sensitivity characteristics of the **a** 4.8-kHz quadrature and **b** 75-Hz in-phase component define the weighting of the subsurface conductivity and susceptibility signal, respectively. Therein, labeled horizontal lines mark the depth integrals that correspond to 10–90% of the EM signal. Selected down-core element contents (**c**–**f**) and rock magnetic parameters (**g**–**j**) are shown for three representative cores with distal (K2), proximal (K3), and central (K5) positions relative to a pockmark

freshwater saturated sediment, which should correspond to a conductivity decline by factors of 3–5 relative to the non-infiltrated surroundings. This estimate matches well with our observed EM conductivities of ca. 0.9 S/m outside and 0.2–0.5 S/m inside the pockmarks (Fig. 6d). Supernatant bottom-water and core bottom pore-water conductivities of all eight investigated gravity cores are compared in Table 1. Relative to the uniform bottom-water conductivities of 3.63–3.72 S/m, all extracted pore-water samples have systematically reduced conductivities at depths of 30–60 cm. Pore-water salinities decrease with proximity to the center of the pockmarks, and reach minimum values of 0.05 S/m in the penetrated sand highs. The data suggest that freshwater has infiltrated the entire Holocene mud drape of

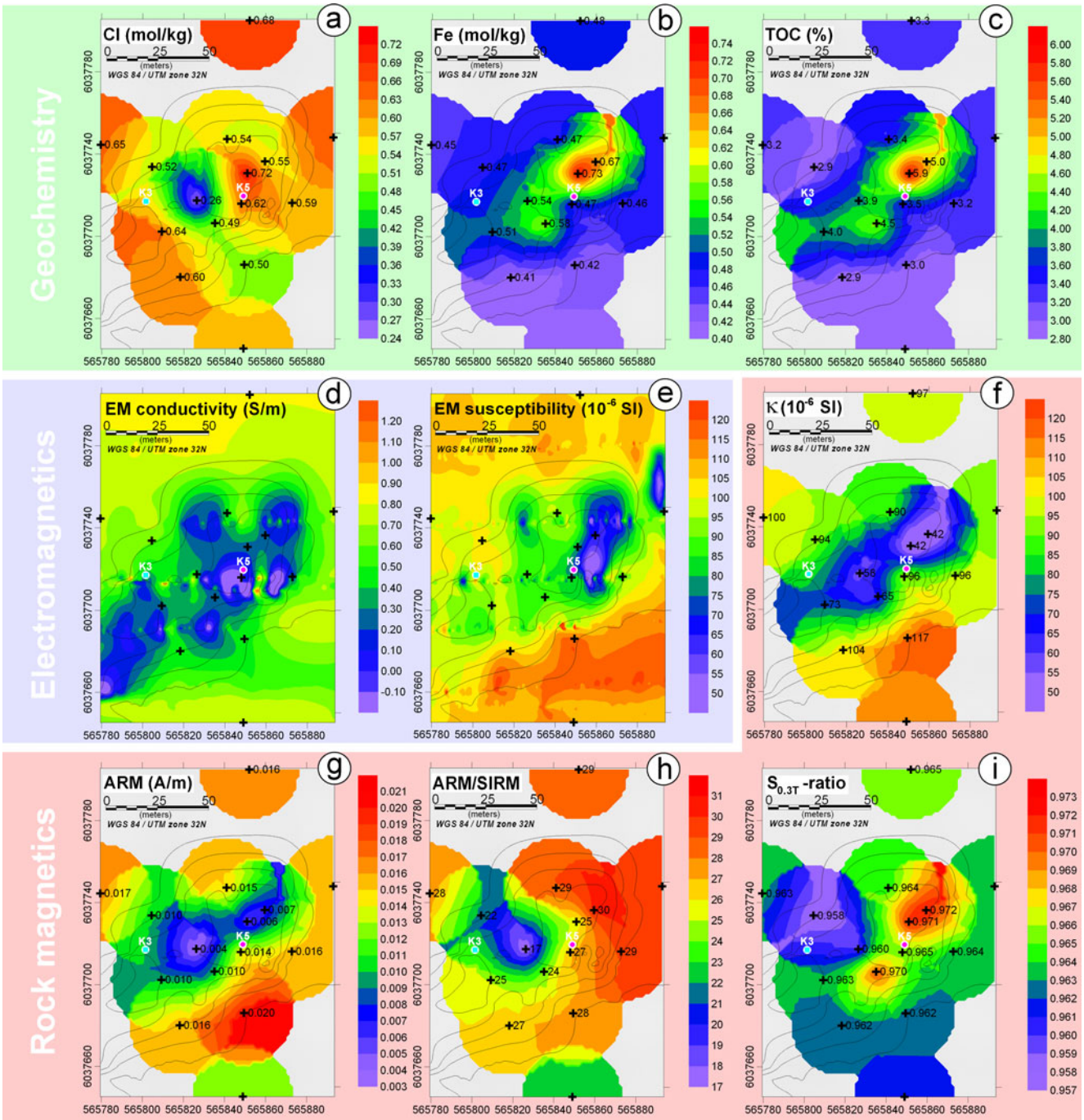

Fig. 6 Surface maps of **a**–**c** element contents and **f**–**i** rock magnetic parameters of 15 grab samples (*crosses*), and **d** EM conductivity and **e** susceptibility for the NE part of pockmark #2. Core locations (K3 and K5) are marked for reference. EM data were gridded using a minimum curvature algorithm; sample data were gridded using a kriging algorithm with a 25-m search radius

the survey area by advection inside the pockmarks, and by diffusive and advective flow outside the pockmarks. Nonlinear Cl^- profiles in Fig. 5c indicate non-steady-state conditions inside pockmarks. Freshwater advection disturbs diffusion by (1) episodically changing hydraulic pressure gradients, (2) seasonally varying bottom-water salinity (Marczinek and Piotrowski 2002), and (3) short-term (e.g., wind-induced) sea-level changes (Whiticar 2002). Focused seepage seems to be indicated by localized bottom- and pore-water conductivity minima (Figs. 3b, 6d), as well as by chloride minima in surface sediments (Fig. 6a).

In contrast to chloride, the dry bulk iron and sulfur contents (Fig. 5d, e) of the distal and proximal cores are almost constant with depth (0.48 and 0.53 mol/kg for Fe, and 0.30 and 0.35 mol/kg for S, respectively). The central core has higher contents of 0.70 mol/kg Fe and 0.42 mol/kg S in the Holocene mud, and much lower contents of 0.28 mol/kg Fe and 0.21 mol/kg S in the glacial sand. Fe/S ratios of 1.59 for the distal, 1.52 for the proximal, and 1.67 (mud) and 1.34 (sand) for the central core indicate that only 30–60% of the iron can occur in a ferrous (Fe^{2+}) sulfidic form such as pyrite (FeS_2; Fe/S=0.5) or mackinawite (FeS; Fe/S=1). Additionally, partly ferric (Fe^{3+}) oxide, oxyhydroxide or silicate iron minerals should be present, which can serve as electron acceptors for organic carbon remineralization. An increase of Fe content is observed toward the center of the pockmark (Fig. 6b), but this could be associated with lateral facies variations, e.g., finer grain sizes and higher clay contents in the pockmarks. There are no obvious indications of prominent Fe depletion, mobilization or precipitation by a freshwater source.

The TOC profiles (Fig. 5f) are strikingly similar to the Fe and S profiles. Observed mean values of 3.1% for the distal, 3.9% for the proximal, and 5.4% (mud) and 0.5% (sand) for the central core are consistent with earlier data on TOC contents of Eckernförde Bay muds of 4–5% at 0–200 cm depth and 7% below 200 cm (Whiticar 2002). Like Fe and S, the TOC content of the surface sediments nearly doubles toward the center of the pockmark (Fig. 6c). This trend could be due to different organic carbon preservation (Whiticar 2002). Organic carbon remineralization requires downward diffusion of sulfate, nitrate or oxygen, which is inhibited by anoxic freshwater advection from below; only the distal core developed a vertical TOC gradient, which is an indication of top-down oxidation, not disturbed by advection.

Down-core magnetic susceptibility profiles (Fig. 5g) of the distal, proximal, and central cores have seafloor values of ~95, 70 and 40×10^{-6} SI, respectively, i.e., increasing values with distance from the seep, as implied by EM- and sample-based surface susceptibility plots (Fig. 6e, f). The distal core has a linear susceptibility decrease with depth from 95 down to 35×10^{-6} SI, while values in the proximal core fluctuate around their mean of 70×10^{-6} SI. The central core has a more complex succession: after a gentle down-core increase from 40 to 50×10^{-6} SI in the upper 0–30 cm, susceptibility declines to 25×10^{-6} SI immediately above the mud/sand boundary at 43 cm, and rises more than tenfold to a stable level of ~350×10^{-6} SI in the glacial sand facies. Given a typical sensitivity of the EM sensor (Fig. 5a), 84% of the EM-based susceptibility signal relates to the weakly magnetic Holocene mud and only 16% to the strongly magnetic glacial base. As a consequence, the positive contribution of glacial sand to the integral EM-based susceptibility signal is not large enough to reverse the negative surface trend, but is reflected in the discrepant values of EM- and surface sample-based magnetic susceptibilities.

The rock magnetic measure for the concentration of the coarser magnetite fraction (>1 μm), SIRM (not shown), indicates nearly the same characteristics as κ both stratigraphically and in map-view. Hysteresis ratios that indicate coarse magnetic particles of $M_{rs}/M_s \leq 0.1$ and $B_{cr}/B_c > 4$ emphasize that the multi-domain (MD) fraction is dominant (Day et al. 1977), and that MD magnetite is most likely the main carrier of the susceptibility signal. This finding is further confirmed by a single low-temperature phase transition at ~120 K known as Verwey transition (Verwey 1939), which is indicative of relatively pure magnetite. The down-core concentration of the finer (0.03–1 μm) single domain (SD) magnetite fraction is represented by the ARM plots (Figs. 5h, 6g). In contrast to depth variations of IRM and κ, the ARM profiles for all three cores decrease sharply by 60–80% within the uppermost 5 cm of the sediment column. This well-known decrease in submicron magnetite at shallow depths is generally attributed to reductive dissolution of ferric Fe oxides below the Fe(II)/Fe(III) redox boundary, and therefore marks the upper limit of the suboxic zone (Berner 1981). This magnetite depletion is driven by the relatively high TOC content of the Holocene mud.

Coincidental shifts of the concentration-independent magnetic grain-size estimate ARM/IRM (Figs. 5i, 6h) and the magnetite/hematite ratio $S_{0.3T}$ (Figs. 5j, 6i) support these findings (Dillon and Bleil 2006; Rowan et al. 2009). The ARM/IRM and $S_{0.3T}$ levels in the central core K5 remain low through the mud/sand boundary, which suggests that the main magnetic carrier of both facies is coarse detrital magnetite of glacial origin, although in much lower concentrations than in the Holocene mud. Distal core K2 seems to have undergone the most pervasive diagenesis at depths below 30 cm, as reflected by the lowest κ and IRM values, the largest shifts in $S_{0.3T}$, and a reversing ARM/SIRM trend. This suggests that even the coarse detrital magnetite fraction is dissolving and only fine-grained

Table 1 Supernatant bottom-water and core bottom pore-water conductivities of eight investigated gravity cores

Core	Position relative to pockmark	Water depth (m)	Bottom-water conductivity (S/m)	Core length (m)	Pore-water conductivity (S/m)	Integrated down-core conductivity decrease
K1	Center	24.5	3.72	0.34	0.05	99%
K2	Distal	23.2	3.71	0.52	1.27	66%
K3	Proximal	23.0	3.72	0.54	0.13	97%
K4	Proximal	24.2	3.69	0.50	1.47	60%
K5	Central	24.2	3.60	0.50	0.06	98%
K6	Distal	23.0	3.77	0.58	1.19	68%
K7	Proximal	23.4	3.63	0.60	0.13	96%
K8	Proximal	23.0	3.69	0.56	0.60	84%

magnetite inclusions in silicate matrix, as well as Ti-rich (hence Fe^{3+}-poor and reduction-resistant) Fe oxides can survive (Dillon and Bleil 2006). We can reasonably deduce from all of our results that all muddy sediments from the deeper bay should be sub- to anoxic and Fe-reducing below 5–10 cm depth irrespective of seepage.

Discussion

Controlling factors for sediment conductivity and susceptibility

The two physical property measurements derived from marine EM differ fundamentally, insofar as electrical conductivity relates primarily to the fluid-filled pore space and magnetic susceptibility to the solid sediment matrix. Conductivity of salt-water saturated samples is controlled by pore-water salinity, porosity, and temperature, while susceptibility depends on ferro-, ferri-, para- and diamagnetic mineral content. The only parameter that affects both properties directly is porosity ϕ, which correlates positively with electrical conductivity:

$$\sigma_{\text{sed}} \cong \sigma_{\text{water}}\phi^{m};\ 1.5 < m < 3 \quad (1)$$

and negatively with magnetic volume susceptibility:

$$\kappa_{\text{sed}} = (1-\phi)\kappa_{\text{matrix}} + \phi\kappa_{\text{water}};\ \kappa_{\text{water}} < 0 << \kappa_{\text{matrix}} \quad (2)$$

For sediments with constant pore-water conductivity and matrix susceptibility, but varying porosity, an inverse nonlinear relation between sediment conductivity and susceptibility should be expected:

$$\frac{\kappa_{\text{sed}}}{\kappa_{\text{matrix}}} \approx 1 - \left(\frac{\sigma_{\text{sed}}}{\sigma_{\text{water}}}\right)^{1/m} \quad (3)$$

The observed down-core decrease in pore-water conductivity by 60–99% in our eight studied gravity cores (Table 1) rules out any assumption of constant pore-water salinity for the study area. This finding is supported by the electrical conductivities measured by the EM sensor at pockmark #2 sampling locations, which are much lower than expected (Eq. 1) for the given porosity of the surface samples (Fig. 7a). Surface susceptibilities correlate negatively with porosity (Fig. 7b), but do not follow a single linear trend, which implies that any assumption of constant bulk susceptibility is also inappropriate here. Matrix (=dry bulk) susceptibilities of these samples vary by a factor exceeding 2 between 250 and 600×10^{-6} SI. Samples from the pockmark centers have systematically lower bulk susceptibilities and higher porosities than do proximal and distal samples, which suggests alteration of the ferrimagnetic mineral fraction by freshwater seepage and fining of the sediment matrix within the pockmarks. Detrital magnetite has typical crystal sizes of <50 μm and is therefore preferentially enriched in finer sediments (Booth et al. 2005; Ellwood et al. 2006), which typically also have higher porosities. Porosity, grain size, and diagenesis should therefore be key controlling factors of sediment susceptibility.

So far, we have regarded the simple case, where the mud layer is taken as a homogeneous half-space. The Eckernförde Bay setting is better described by a two-layer model composed of a finite Holocene mud layer of 0–5 m thickness on top of a semi-infinite glacial base. In the two cores that reach the glacial base, the pore-water conductivity at the core bottom has near-freshwater values of 0.05 S/m, porosity is about 50%, and susceptibility is 350×10^{-6} SI. The Holocene mud was modeled (two-layer model; Müller 2010) with pore-water conductivities ranging from 0.05 to 2.6 S/m, sediment susceptibilities from 20 to 100×10^{-6} SI, and a mean porosity of 80% (Fig. 7c, d). The two sets of curves model the EM response for discrete mud conductivities and susceptibilities as a function of mud layer thickness. With diminishing thickness of the Holocene drape, the contrasting glacial base shifts the surface conductivities to lower values and susceptibilities to higher values. The base starts

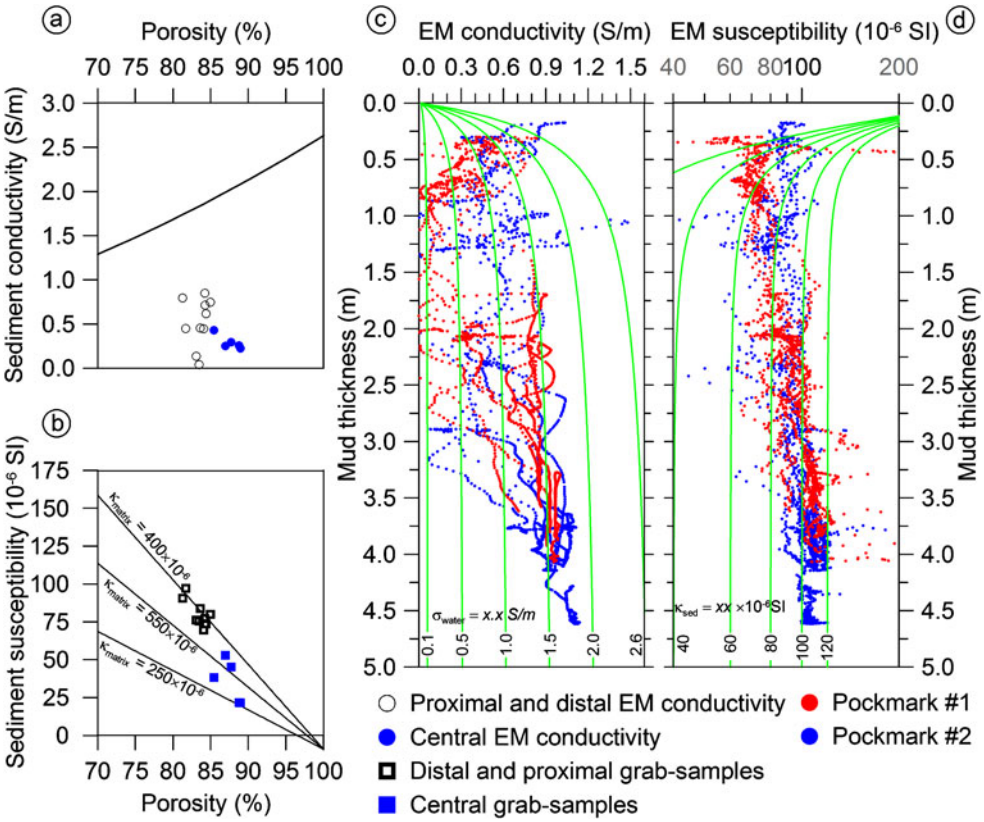

Fig. 7 **a** For given surface sample porosities, the respective EM sediment conductivity values are generally much lower than theoretically expected (solid line calculated using Eq. 1 with m=2). **b** Susceptibility values of proximal and distal samples scatter around the theoretical curve for $\kappa_{matrix}=550\times10^{-6}$ SI (Eq. 2), while low central pockmark susceptibilities could not be explained by reduced porosity. **c** EM conductivity and **d** susceptibility of pockmarks #1 and #2 increase with Holocene mud thickness. Two-layer models for various values of σ_{mud} and κ_{mud} over sand (ϕ=50%, $\kappa=350\times10^{-6}$ SI) are shown by *green lines*

to have a noticeable influence on EM measurements at depths above 3 m, becomes critical above 1 m, and dominant above 50 cm. This effect is mainly due to the relatively large transmitter coil diameter of 96 cm. It could be reduced by decreasing the coil size—however, at the cost of higher noise from seafloor roughness.

By plotting real EM data from pockmarks #1 and #2 onto both model curves (Fig. 7c, d), some important conclusions can be drawn.

- EM conductivity data indicate larger scatter and hence higher lateral variability than do the EM susceptibility data, which may have various reasons. First, pore-water salinity near freshwater seeps can change by several orders of magnitude, whereas sediment susceptibility cannot be reduced by so much due to mineralogical limitations. Second, conductivity mirrors the current, spatially complex and temporally dynamic hydrological system, while alteration of the magnetic mineral fraction is a slower chemical process proceeding in periods of several years (Emiroglu et al. 2004). Salinity change is reversible, magnetic mineral depletion is not. Third, focused freshwater flow has high impact on (local) conductivity, while magnetic mineral reduction occurs with focused as well as with diffuse flow.
- Model susceptibility curves are curvilinear at the top and converge to constant mud values at ca. 3 m depth, while the EM trends are nearly linear throughout the 5 m depth range and have a pronounced gradient. With decreasing mud layer thickness, susceptibilities shift toward more reduced states. It is also noteworthy that the data trends for pockmarks #1 and #2 have different gradients and continuously change at depths exceeding 3 m, which is the theoretical detection limit of the glacial base.
- EM conductivities shift in general toward freshwater saturation with decreasing mud layer thickness, although localized conductivity minima, i.e., seep centers, are not restricted to areas of smallest mud thickness. Hydraulic gradients and sub-bottom conduits may be more decisive for their localization.

The shifting of σ and κ with mud thickness is therefore not a direct geometrical effect, but is rather the result of an indirect geological process: a thinner and therefore more permeable mud layer facilitates freshwater infiltration from the basal aquifer. As a result, mud porosity increases and susceptibility decreases. The theoretical possibility of positive susceptibility anomalies over (near) outcropping sand highs is not observed in practice.

Freshwater seepage and magnetic mineral diagenesis

Geochemical and rock magnetic data from surface and core samples shown above (Figs. 5, 6) provide qualitative

evidence that grain-size and diagenetic effects are the main causes of negative susceptibility anomalies around Eckernförde Bay pockmarks. We present rank-order correlation statistics of magnetic susceptibility versus selected geochemical and rock magnetic parameters (Fig. 8) to substantiate this interpretation. The presented theory and statistical analysis (Fig. 7) suggest that higher porosities of pockmark sediments should at least partly account for the lowering of susceptibility. Porosity is negatively correlated with susceptibility, while chloride content has a statistically insignificant relationship, most likely because salinity fluctuations due to advective and diffusive processes are magnetically irrelevant. The highly significant positive correlation of susceptibility with SIRM (magnetite), anti-correlation with Fe content (paramagnetic iron), and a distinct Verwey transition identify magnetite as carrier of the susceptibility signal. The positive significant correlation of κ and Si/Al indicates higher magnetite concentrations in the coarser quartz-rich intervals, and lower concentrations in the finer clay-rich sediments. Clay minerals conserve a larger pore space, which 'dilutes' also the magnetic fraction and reduces volume susceptibility.

Higher TOC contents within the pockmarks can result from calmer settling conditions, as well as from better preservation in surface sediments due to lower oxygenation and hence reduced remineralization. TOC has a high negative correlation with susceptibility. Reactive organic carbon, methane and sulfate drive the suboxic and/or sulfidic dissolution of ferrimagnetic Fe oxides and the precipitation of paramagnetic Fe sulfides (Berner 1981; Fu et al. 2008) by the following reactions: $2Fe_3O_4 + CH_2O + 11H \rightarrow 6Fe^{2+}_{(aq)} + HCO^-_3 + H_2O$ (magnetite dissolution by organic matter), $CH_4 + SO^{2-}_4 \rightarrow HCO^-_3 + H_2O + HS^-$ (formation of hydrogen sulfide from methane and sulfate), $Fe_3O_4 + HS^- + 7H^+ \rightarrow 3Fe^{2+}_{(aq)} + S^0_{(s)} + 4H_2O$ (magnetite dissolution by hydrogen sulfide), $Fe^{2+}_{(aq)} + HS^- \rightarrow FeS_{(s)} + H^+$ (precipitation of dissolved iron by hydrogen sulfide).

Total Fe and (porosity-independent) diagenesis indices Fe/Al (Fe precipitation) and S/Al (pyritization) are therefore elevated within the pockmarks, but correlate negatively with κ, which suggests that only paramagnetic Fe species are precipitated from the anoxic, Fe^{2+}-rich (ca. 2 mg/l; Marczinek and Piotrowski 2002) freshwater. Precipitation of weakly magnetic secondary iron minerals by diagenesis and seepage hence does not contribute significantly to magnetic susceptibility. As in many other reductive marine environments (e.g., Zhang et al. 2001; Tribovillard et al. 2002; Emiroglu et al. 2004), diagenetic dissolution of the strongly magnetic primary magnetite phase is the predominant, statistically most significant process.

The best evidence for magnetite dissolution is provided by rock magnetic parameters. Total loss of fine-grained magnetite below the Fe redox boundary is detected by ARM/IRM (Figs. 5i, 8b), which correlates significantly with the susceptibility decrease. Better preservation of hematite vs. magnetite ($S_{0.3T}$) and shifts in the proportion of para- and ferrimagnetic iron (Fe/χ) are recognized fingerprints of magnetite depletion (Funk et al. 2004). This process is active within the entire Holocene drape, but is more pervasive in and near the pockmarks.

The high data quality and excellent consistency of acoustic pockmark morphologies with EM conductivity and susceptibility images (Fig. 3), supported by our reasoning for signal formation in which we invoke an interaction of episodic freshwater advection and long-term iron mineral diagenesis, form a solid framework to use EM data for sediment classification. In order to demonstrate the lithostratigraphic potential of EM fingerprinting, the main structural elements of the Eckernförde Bay study area (basin, rise, slope, and pockmarks #1 to #5) have been

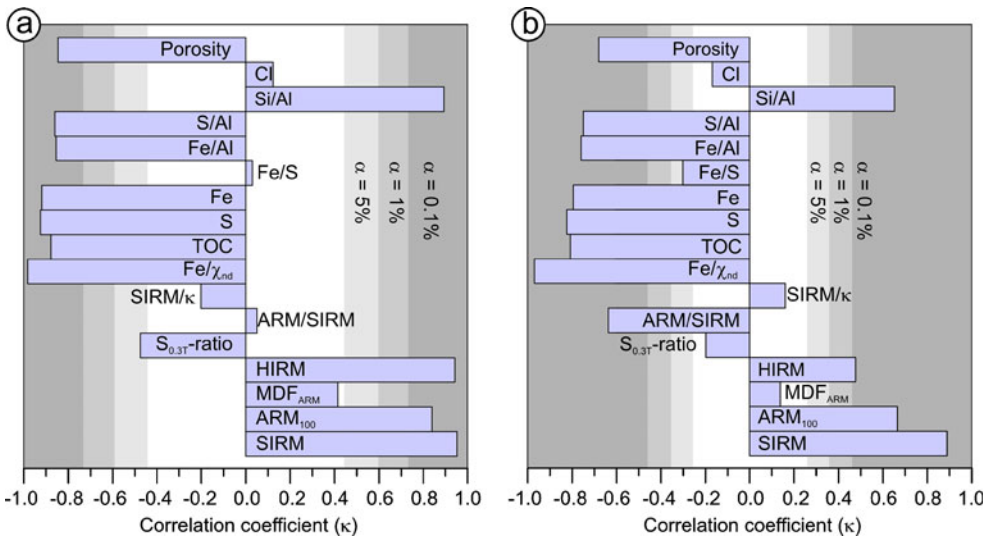

Fig. 8 Spearman rank-order correlation statistics of magnetic susceptibility versus a set of geochemical and rock magnetic parameters from **a** surface samples and **b** core samples. Levels of significance are α=0.1% (highly significant), 1%, and 5%

grouped and color-coded (Fig. 9d). Dispersed metal objects (e.g., scrap metal, ordnance) deviate from the geological background by their unusually high susceptibility (Figs. 3f, 9b, c), and were identified and grouped by a threshold method.

When plotted against water depth (Fig. 9a), background conductivity is uniform on the slope (yellow) and increases slightly with porosity toward the rise (orange) and basin (brown). Pockmarks #1 (red, 24 m), #2 (blue, 23–25 m), #3 and #4 (green, 22–23 m), and #5 (green, 19–21 m) protrude sharply from the main trend by their reduced conductivities due to freshwater infiltration. In the same representation (Fig. 9b), background magnetic susceptibility has much higher sensitivity to sediment lithology, i.e., magnetic mineral content, grain size, and porosity. Metallic contaminants are easily identified as positive outliers, while the negative scatter by early diagenetic alteration appears quite modest on linear axis scaling. From the susceptibility to depth trend (dashed line in Fig. 9b), susceptibility values within pockmarks are higher than for basin sediments at comparable depths. Thus, susceptibility alone is not capable of classifying the sediment correctly. A bivariate scatter plot of susceptibility against conductivity (Fig. 9c) greatly expands the discriminative power of EM imaging. Three main trends can be discerned.

1. The lithological variability of the Holocene drape sediment is determined by clay content, which determines grain size and porosity. Under the specific local settings, sediment fining is associated with a pronounced decrease of susceptibility and a somewhat lesser increase in conductivity, in accordance with Eq. 1. This signal formation process is responsible for the discrimination of slope, rise and basin sediments (Figs. 3e, f, h and 9c, d), and the depth dependence of κ and σ (Fig. 9a, b).

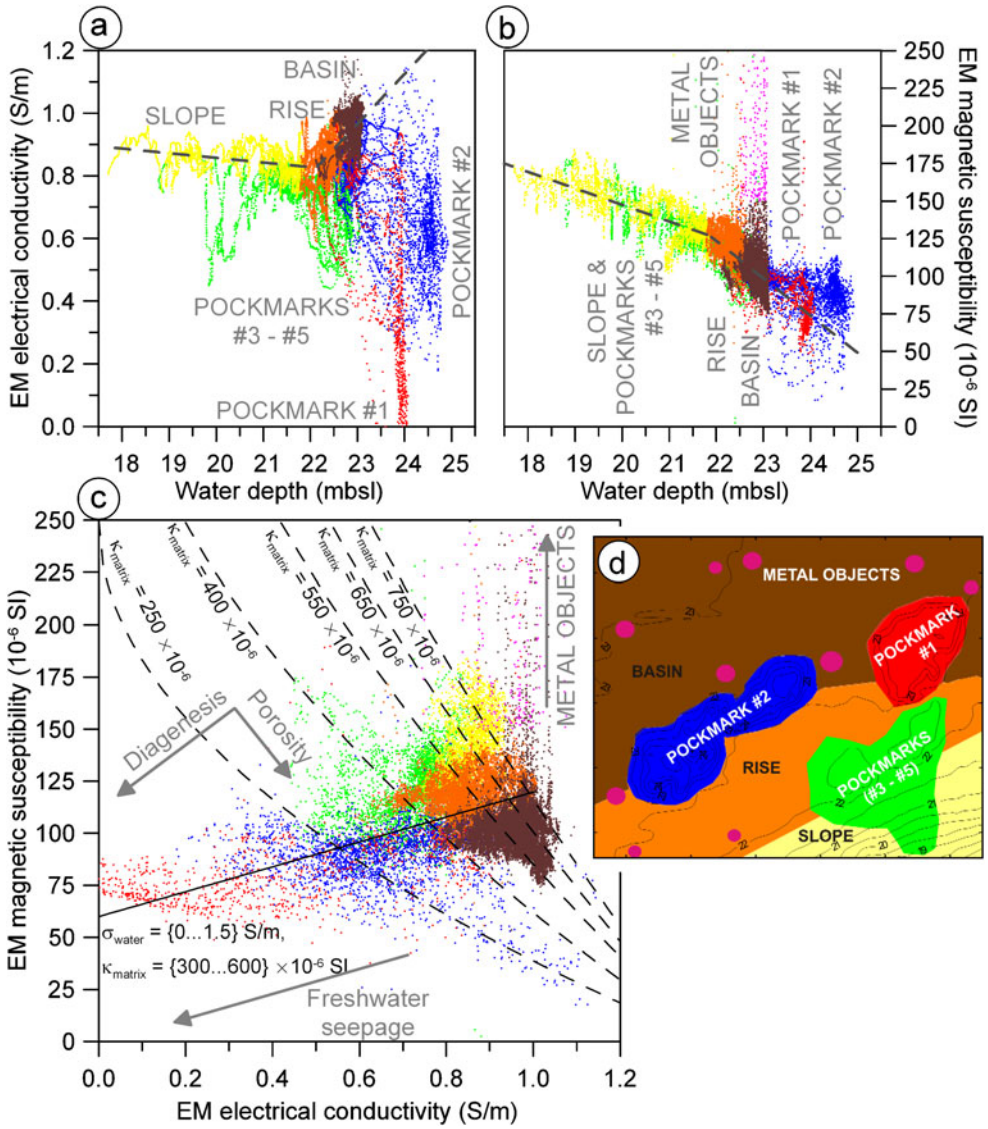

Fig. 9 EM fingerprinting of sediments in the study area. The main structural elements (basin, rise, slope, and pockmarks #1 to #5) are depicted in the bathymetric map (**d**) and are color coded. Ferrous metal objects identified were grouped using a threshold method. Linear trends are given for **a** conductivity to depth, and **b** susceptibility to depth relations of slope, rise, and basin sediments (*dashed lines*). **c** Sediment data in the susceptibility versus conductivity plot have porosity trends (*dashed lines*) shown for a constant pore-water conductivity of 1.4 S/m and varying values of matrix susceptibility κ_{matrix} following Eq. 3 (m=2). The freshwater trend (*solid line*) is given by parametric equations analogous to Eqs. 1 and 2: $\sigma(t) = (1 - 100/550)^2 t$ and $\kappa(t) = 200(t + 1.5)(1 - 0.8)$; t={0 ... 1.5}

2. Freshwater seepage is represented by a major decline of conductivity (salinity) along with a minor decrease in susceptibility (diagenesis; Fig. 9c). According to these trends, the pockmark structures #1, #2, and #3–#5 differ in grain size (e.g., #2 is muddier than #3–#5) and freshwater saturation (e.g., #1 is less saline than #2), as well as in the pervasiveness of magnetite depletion. Freshwater advection therefore reduces sediment susceptibility by a combination of pore-water injection and magnetite depletion.
3. Ferromagnetic metal objects along or beside the sled tracks have 4–6 orders of magnitude higher intrinsic susceptibilities and conductivities than the surrounding sediment. Because of geometry and frequency effects, metal detection by the 75-Hz susceptibility measurement is much more efficient than by the 4.8-kHz conductivity measurement (Figs. 3e, f, 9a–c). Depending on the volume and distance of metallic objects, apparent susceptibilities rise locally by more than 400×10^{-6} SI. Alternatively, such localized highly magnetic spots might represent ferrimagnetic iron sulfide (greigite) nodules, which have been encountered with cold seeps and marine sediments where anaerobic oxidation of methane occurs (Roberts and Weaver 2005; Larrasoaña et al. 2007; Van Dongen et al. 2007). According to our modeling, a greigite nodule of 5 cm size and a susceptibility of 0.5 SI (Dekkers and Schoonen 1996) located at 5 cm sediment depth below the sensor track would cause a magnetic susceptibility anomaly of 600×10^{-6} SI (160×10^{-6} SI at a depth of 20 cm). However, a presence of sulfide nodules could not be confirmed and has never been reported for this site.

Conclusions

Seepage of fresh, anoxic groundwater in Eckernförde Bay has a major effect on the pore-water salinity and magnetic mineralogy of the affected surface sediments (Fig. 10). The affinity of electrical conductivity to pore-water salinity and temperature enables us to use bottom-towed CSEM profiling to map the recent state of freshwater distribution in the sediment resulting from vertical advection and lateral diffusion processes. Associated anomalies of magnetic susceptibility distribution are related to the solid phase mineralogy of the sediment, and reflect the diagenetic impact of fluid seepage over sufficiently long past or present periods necessary to dissolve primary magnetic iron minerals. Magnetic susceptibility minima within pockmarks maintain their position relative to sand highs underneath.

Our study demonstrates that the spatial interpretation of punctual data from sediment samples is unable to precisely delineate the structures, and is prone to misleading interpolation errors and unrecognized outliers. EM mapping opens the possibility to create detailed fingerprint images of surface sediment alteration by submarine freshwater seeps. Bivariate plots of EM susceptibility versus conductivity data can also clearly distinguish lithofacies and hydrofacies units of slope, rise and basin, and pockmark sediments. Because of the depth-integrating nature of the EM signal,

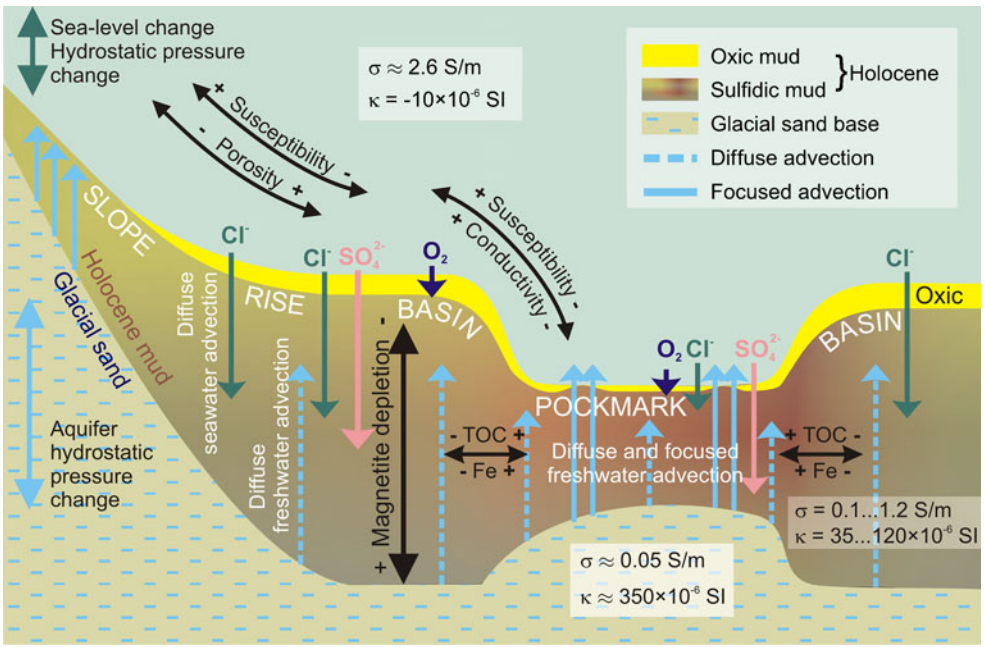

Fig. 10 Conceptual hydrogeological model of near-surface sedimentary units, freshwater advection, element exchange, and Fe oxide depletion in Eckernförde Bay. Focused and diffusive freshwater advection within pockmarks reduces the magnetic sediment susceptibility by a combination of pore-water injection and magnetite depletion. Seepage and subsequent pockmark formation is related to the thinned Holocene mud drape above glacial sand highs

core-based geochemical and rock magnetic data remain essential to assess and explain the vertical zonation of seepage-related processes.

The results of this study imply that near-surface electromagnetic profiling can significantly improve our understanding of sediment distribution and submarine groundwater discharge. This rapid and cost-effective method still bears large potential for further improvement by using multi-coil EM systems enabling higher resolution and depth inversion.

Acknowledgements Four survey campaigns with the RB *Polarfuchs* in the Western Baltic Sea were granted by IfM GEOMAR in Kiel and Center for Marine Environmental Sciences (MARUM) at the University of Bremen. We thank the ship's crew members H. Meier and H. Schramm for their great support. We also thank C. Hilgenfeldt and T. Frederichs for technical assistance, and D. Rey, B. Rubio, G. Bohrmann, F. Abegg, I.J. Won, B. SanFilipo, and M. Schlüter for thoughtful suggestions and comments. The authors would like to thank A. Roberts and B. Housen for helpful comments in their detailed reviews of the manuscript. Research, development, and implementation of the electromagnetic seafloor profiler *Neridis II* was jointly funded by MARUM incentive funding and two research grants of the Marine and Environmental Geology Group (MARGO) at the University of Vigo (Spain), PGDIT06TAM31201PR (XUGA) and CTM 2007-61227/MAR (micinn). This work contributes to MARUM projects C1 and SD2 on sediment dynamics.

References

Archie GE (1942) The electrical resistivity log as an aid in determining some reservoir characteristics. J Petrol Technol 5:1–8

Benech C, Marmet E (1999) Optimum depth of investigation and conductivity response rejection of the different electromagnetic devices measuring apparent magnetic susceptibility. Archaeol Prospection 6:31–45

Berner RA (1981) A new geochemical classification of sedimentary environments. J Sed Petrol 51:359–365. doi:10.1306/212F7C7F-2B24-11D7-8648000102C1865D

Bloemendal J, King JW, Hall FR, Doh SJ (1992) Rock magnetism of late Neogene and Pleistocene deep-sea sediments: relationship to sediment source, diagenetic processes, and sediment lithology. J Geophys Res 97:4361–4375. doi:10.1029/91JB03068

Booth CA, Walden J, Neal A, Smith JP (2005) Use of mineral magnetic concentration data as a particle size proxy: a case study using marine, estuarine and fluvial sediments in the Carmarthen Bay area, South Wales, U.K. Sci Total Environ 347:241–253. doi:10.1029/91JB03068

Burnett WC, Taniguchi M, Oberdorfer J (2001) Measurement and significance of the direct discharge of groundwater into the coastal zone. J Sea Res 46:109–116. doi:10.1016/S1385-1101(01)00075-2

Burnett WC, Aggarwal PK, Aureli A et al (2006) Quantifying submarine groundwater discharge in the coastal zone via multiple methods. Sci Total Environ 367:498–543. doi:10.1016/j.scitotenv.2006.05.009

Day R, Fuller M, Schmidt VA (1977) Hysteresis properties of titanomagnetites: grain-size and compositional dependence. Phys Earth Planet Interiors 13:260–266. doi:10.1016/0031-9201(77)90108-X

Dekkers MJ, Schoonen MAA (1996) Magnetic properties of hydrothermally synthesized greigite (Fe_3S_4) - I. Rock magnetic parameters at room temperature. Geophys J Int 126:360–368

Dillon M, Bleil U (2006) Rock magnetic signatures in diagenetically altered sediments from the Niger deep-sea fan. J Geophys Res 111:B03105. doi:10.1029/2004JB003540

Dunlop DJ, Özdemir Ö (1997) Rock magnetism: fundamentals and frontiers. Cambridge Studies in Magnetism. Cambridge University Press, Cambridge

Ellwood BB, Balsam WL, Roberts HH (2006) Gulf of Mexico sediment sources and sediment transport trends from magnetic susceptibility measurements of surface samples. Mar Geol 230:237–248. doi:10.1016/j.margeo.2006.05.008

Emiroglu S, Petersen N, Rey D (2004) Magnetic properties of sediment in the Ría de Arousa (Spain): dissolution of iron oxides and formation of iron sulphides. Phys Earth Planet Interiors 29:947–959. doi:10.1016/j.pce.2004.03.012

Evans ME, Heller F (2003) Environmental magnetism. Principles and applications of enviromagnetics. Academic, New York

Farquharson CG, Oldenburg DW, Routh PS (2003) Simultaneous 1D inversion of loop–loop electromagnetic data for magnetic susceptibility and electrical conductivity. Geophysics 68:1857–1869

Fu Y, von Dobeneck T, Franke C, Heslop D, Kasten S (2008) Rock magnetic identification and geochemical process models of greigite formation in Quaternary marine sediments from the Gulf of Mexico (IODP Hole U1319A). Earth Planet Sci Lett 275:233–245. doi:10.1016/j.epsl.2008.07.034

Funk JA, von Dobeneck T, Reitz A (2004) Integrated rock magnetic and geochemical quantification of redoxomorphic iron mineral diagenesis in Late Quaternary sediments from the Equatorial Atlantic. In: Wefer G, Mulitza S, Ratmeyer V (eds) The South Atlantic in the Late Quaternary: reconstruction of material budget and current systems. Springer, Berlin Heidelberg, pp 237–260

Gay SP (2004) Glacial till: a troublesome source of near-surface magnetic anomalies. Lead Edge 23:542–547

Harrington PK (1985) Formation of pockmarks by pore-water escape. Geo-Mar Lett 5(3):193–197. doi:10.1007/BF02281638

Hoefel FG, Evans RL (2001) Impact of low salinity pore water on seafloor electromagnetic data: a means of detecting submarine ground water discharge? Estuarine Coastal Shelf Sci 52:179–189. doi:10.1006/ecss.2000.0718

Housen BA, Moskowitz BM (2006) Depth distribution of magnetofossils in near-surface sediments from the Blake/Bahama Outer Ridge, western North Atlantic Ocean, determined by low-temperature magnetism. J Geophys Res 111:G01005. doi:10.1029/2005JG000068

Housen BA, Musgrave RJ (1996) Rock-magnetic signature of gas hydrates in accretionary prism sediments. Earth Planet Sci Lett 139:509–519. doi:10.1016/0012-821X(95)00245-8

Hovland M (2003) Geomorphological, geophysical, and geochemical evidence of fluid flow through the seabed. J Geochem Explor 78(79):287–291. doi:10.1016/S0375-6742(03)00091-8

Hussenoeder SA, Tivey MA, Schouten H (1995) Direct inversion of potential fields from an uneven track with application to the Mid-Atlantic Ridge. Geophys Res Lett 22:3131–3134. doi:10.1029/95GL03326

Jensen JB, Kuijpers A, Bennike O, Laier T, Werner F (2002) New geological aspects for freshwater seepage and formation in Eckernförde Bay, western Baltic. Cont Shelf Res 22:2159–2173. doi:10.1016/S0278-4343(02)00076-6

Karpen V, Thomsen L, Suess E (2004) A new 'schlieren' technique application for fluid flow visualization at cold seep sites. Mar Geol 204:145–159. doi:10.1016/S0025-3227(03)00370-0

King JW, Channell JET (1991) Sedimentary magnetism, environmental magnetism, and magnetostratigraphy. Rev Geophys 29:358–370

King J, Banerjee SK, Marvin J, Özdemir Ö (1982) A comparison of different magnetic methods for determining the relative grain size of magnetite in natural materials: some results from lake sediments. Earth Planet Sci Lett 59:404–419. doi:10.1016/0012-821X(82)90142-X

Larrasoaña JC, Roberts AP, Musgrave RJ, Gracia E (2007) Diagenetic formation of greigite and pyrrhotite in gas hydrate marine sedimentary systems. Earth Planet Sci Lett 261:350–366. doi:10.1016/j.epsl.2007.06.032

Maher BA, Thompson R (1999) Quaternary climates, environments and magnetism. Cambridge University Press, Cambridge

Marczinek S, Piotrowski JA (2002) Groundwater transport and composition in the Eckernforder Bay catchment area, Schleswig-Holstein. Grundwasser 7(2):101–107

Moore WS (1996) Large groundwater inputs to coastal waters revealed by ^{226}Ra enrichment. Nature 380:612–614

Müller H (2010) Characterization of marine near-surface sediments by electromagnetic profiling. Dissertation, Universität Bremen, Bremen

Nehmiz W (2007) Umweltmagnetische und geochemische Untersuchungen an Grundwasseraustritten in der Eckernförder Bucht. Diplomarbeit, Universität Bremen, Bremen

Novosel I, Spence GD, Hyndman RD (2005) Reduced magnetization produced by increased methane flux at a gas hydrate vent. Mar Geol 216:265–274. doi:10.1016/j.margeo.2005.02.027

Oldfield F, Yu L (1994) The influence of particle-size variations on the magnetic properties of sediments from the N.E. Irish Sea. Sedimentology 41:1093–1108

Rey D, Mohamed KJ, Bernabeu A, Rubio B, Vilas F (2005) Early diagenesis of magnetic minerals in marine transitional environments: geochemical signatures of hydrodynamic forcing. Mar Geol 215:215–236. doi:10.1016/j.margeo.2004.12.001

Rey D, Müller H, Rubio B (2008) Using electromagnetic sensors to estimate physical properties and environmental quality of surface sediments in the marine environment. Preliminary results. Geotemas 10:651–654

Roberts AP, Weaver R (2005) Multiple mechanisms of remagnetization involving sedimentary greigite (Fe_3S_4). Earth Planet Sci Lett 231:263–277. doi:10.1016/j.epsl.2004.11.024

Rowan CJ, Roberts AP (2006) Magnetite dissolution, diachronous greigite formation, and secondary magnetizations from pyrite oxidation: unravelling complex magnetizations in Neogene marine sediments from New Zealand. Earth Planet Sci Lett 241:119–137. doi:10.1016/j.epsl.2005.10.017

Rowan CJ, Roberts AP, Broadbent T (2009) Reductive diagenesis, magnetite dissolution, greigite growth and paleomagnetic smoothing in marine sediments: a new view. Earth Planet Sci Lett 277:223–235. doi:10.1016/j.epsl.2008.10.016

Schlüter M, Sauter EJ, Andersen CE, Dahlgaard H, Dando PR (2004) Spatial distribution and budget for submarine groundwater discharge in Eckernforde Bay (western Baltic Sea). Limnol Oceanogr 49:157–167

Seeberg-Elverfeldt J, Schlüter M, Feseker T, Kölling M (2005) Rhizon sampling of porewaters near the sediment-water interface of aquatic systems. Limnol Oceanogr 3:361–371

Siemon B (2006) Airborne techniques. In: Kirsch R (ed) Groundwater geophysics—A tool for hydrogeology. Springer, Berlin Heidelberg, pp 348–362

Steuer A, Siemon B, Auken E (2007) A comparison of helicopter-borne electromagnetics in frequency- and time-domain at the Cuxhaven valley in Northern Germany. J Appl Geophys 67:194–205

Thompson R, Oldfield F (1986) Environmental magnetism. Allen & Unwin, Sydney

Thompson R, Bloemendal J, Dearing JA (1980) Environmental applications of magnetic measurements. Science 207:481–486

Tivey MA, Johnson HP (2002) Crustal magnetization reveals subsurface structure of Juan de Fuca Ridge hydrothermal vent fields. Geology (Boulder, CO) 30:979–982

Tribovillard N, Averbuch O, Bialkowski A, Deconinck JF (2002) Early diagenesis of marine organic-matter and magnetic properties of sedimentary rocks: the role of iron limitation and organic-matter source organisms. Bull Soc Géol France 173:295–306

Van Dongen BE, Roberts AP, Schouten S, Jiang WT, Florindo F, Pancost RD (2007) Formation of iron sulfide nodules during anaerobic oxidation of methane. Geochim Cosmochim Acta 71:5155–5167. doi:10.1016/j.gca.2007.08.019

Verosub KL, Roberts AP (1995) Environmental magnetism: past, present, and future. J Geophys Res 100:2175–2192

Verwey EJW (1939) Electronic conduction of magnetite (Fe_3O_4) and its transition point at low temperatures. Nature 144:327–328

Whiticar MJ (2002) Diagenetic relationships of methanogenesis, nutrients, acoustic turbidity, pockmarks and freshwater seepages in Eckernförde Bay. Mar Geol 182:29–53. doi:10.1016/S0025-3227(01)00227-4

Whiticar MJ, Werner F (1981) Pockmarks: submarine vents of natural gas or freshwater seeps? Geo-Mar Lett 1(3/4):193–199. doi:10.1007/BF02462433

Won IJ, Huang H (2004) Magnetometers and electro-magnetometers. Lead Edge 23:448–451

Won IJ, Keiswetter DA, Hanson DR, Novikova E, Hall TM (1997) GEM-3: a monostatic broadband electromagnetic induction sensor. J Environ Eng Geophys 2:53–64

Zhang W, Yu L, Hutchinson SM (2001) Diagenesis of magnetic minerals in the intertidal sediments of the Yangtze Estuary, China, and its environmental significance. Sci Total Environ 266:160–175. doi:10.1016/S0048-9697(00)00735-X